Audio Engineering Society

Convention Paper 10423

Presented at the 149th Convention
Online, 2020 October 27-30

Acoustic Mass and Resistance as Function of Drive Level for Straight, Bent, and Flared Loudspeaker Ports

Andri Bezzola[1], Glenn S. Kubota[1], and Allan O. Devantier[1]

[1]*Samsung Research America, DMS Audio, Valencia CA 91355*

Correspondence should be addressed to Andri Bezzola (andri.b@samsung.com)

ABSTRACT

Nonlinear control of bass-reflex loudspeakers requires accurate knowledge of acoustic mass and acoustic resistance of the port. The values of these parameters are hard to measure and previous research indicates that they are both functions of turbulence levels in the port airflow. Well-designed ports are known to accept higher drive levels before flow separation and vortex shedding causes unwanted port noise. This work investigates the relationship between dependence of port variables and port noise as functions of drive level. Measurements show that port acoustic mass is essentially a constant independent of drive level, and that port acoustic resistance is related to drive level much in the same way port compression and port noise are. Absence of proper flaring of ports and introduction of bends in ports can both exacerbate the increase of port acoustic resistance with drive level, along with port compression and port noise. A properly flared port - even if it is bent - performs better than a straight unflared port. Straight and optimally flared ports have values of port acoustic mass and resistance that change less than 2 dB from lowest to highest drive levels.

1 Introduction

Bass-reflex ports are popular and effective to increase the low-frequency acoustic output of loudspeakers. At high sound pressure levels, ports can exhibit an unwanted amount of noise and distortion because the air flow becomes turbulent [1, 2, 3] and flow separation can occur, resulting in unwanted port noise [4, 5]. Lumped parameter models of vented boxes require knowledge of port acoustic mass M_{ap} and port acoustic resistance R_{ap} among other values. Empirical studies on acoustic impedance of orifices and Helmholtz resonators dating back as early as 1935 have found that acoustic resistance increases with drive levels and some have found a dependence of mass reactance with drive level [6, 7, 8, 9]. Those studies used orifice geometries that were short relative to their diameter.

Button et al. showed in their 2018 AES Convention paper that M_{ap} and R_{ap} are level dependent for a general bass reflex port [10]. They suggested the use of lookup tables that correlate M_{ap} and R_{ap} with drive level to accurately model the nonlinear behavior of vented boxes with lumped parameter (LP) simulations. This creates a computational overhead when the LP are used in nonlinear control algorithms, because the values of M_{ap} and R_{ap} were dependent on the calcula-

tion of the envelope of drive level. The ports used in that study had shapes that were suboptimal from a fluid dynamics point of view and some resembled an orifice, rather than a tube. In the latest 2020 AES Convention in Vienna, Pene et al. presented computational fluid dynamics simulation and acoustic measurements on loudspeaker ports that showed that unflared ports had much higher nonlinear losses than a flared port at high drive levels [11].

Based on the groundbreaking work of Vanderkooy [2], Backman [1], Roozen [4], Salvatti [3], and others in the 1990s and early 2000s, we have previously presented a method based on finite element (FE) simulations to calculate flared port profiles for which the onset of turbulence occurs at highest possible drive levels [12]. Such ports had optimized flare rates that minimize the propensity for flow separation and the excitation of unwanted port eigenfrequencies. In that work, we showed that suboptimal ports exhibit flow separation and vortex shedding already at very low levels. In that paper we also showed that propensity for flow separation and vortex shedding correlates well with listeners' perception of port sound quality.

Most port research has been conducted with straight ports, but in his earliest paper on nonlinear port behavior, Backman showed that bent ports exhibit stronger compression than their straight counterparts, noting that "only smooth bends should be safely used in reflex ports" [1]. He made this observation based on distortion and compression measurements. In this work we attempt to link the observed port compression measurements from [1] and [11] to changes in port parameters M_{ap} and R_{ap}. In the following sections, we will explain how we designed a series of six ports and how we estimated M_{ap} and R_{ap} for those six ports at different drive levels.

2 Methods

2.1 Port Geometries and Driver T/S Parameters

We have designed a series of six ports to investigate the influence of flaring and bending ports on port resistance and mass. Ports **A** thru **E** have a physical length of $L_{port} = 120$ mm and the sixth port **F** has a length of $L_{port} = 150$ mm. Ports **A**, **B**, and **C** have a constant diameter, while ports **D**, **E**, and **F** were designed to have optimal flare ratio according to the design method described by the authors in an earlier paper [12]. Ports

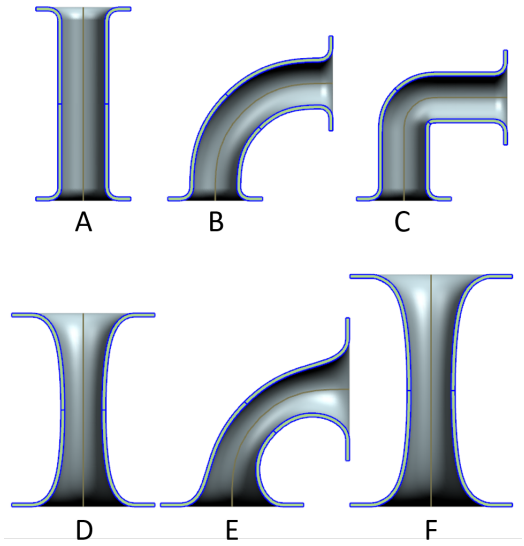

Fig. 1: Longitudinal cross section for ports **A** thru **F**.

A, **D**, and **F** have a straight center line, and ports **B**, **C**, and **E** have a 90° bend of radius R_{bend} at the center of the port. Port **C** has a maximally sharp R_{bend} and ports **B** and **E** have a maximally gentle R_{bend}. All ports are designed with a 10-mm blend radius at port exits, as well as a 20-mm flange on the free ends. The geometric features of the ports are summarized in Table 1, and cross-sectional profiles along port axis are shown in Figure 1.

To drive the system, we chose a 6.5-inch woofer in a 12-L box. To characterize the woofer, we measured it with the laser version of the Linear Parameter Measurement (LPM) and Large Signal Identification (LSI) modules of the Klippel Analyzer System [13] in free air. The measured linear Thiele-Small (T/S) parameters of the 6.5-inch woofer are given in table 2, the large-signal parameters are shown in Figure 2, and the predicted system alignment of the ports and drivers in a 12-L box are shown in Figure 3. The port tuning frequency is at 36.5 Hz, resulting in a well-tuned vented-box system with a compliance ratio of $\alpha = V_{as}/V_{ab} = 1.12$ and a tuning ratio of $h = f_b/f_s = 0.98$.

2.2 Lumped Parameter Model

The linear and nonlinear LP models both have the same state-space structure that is discussed below. In the nonlinear case, Bl, K_{ms}, and L_e become functions of

Port	L_{port} [mm]	D_c [mm]	D_e [mm]	R_{bend} [mm]
A	150	33.4	33.4	∞
B	150	33.4	33.4	90.7
C	150	33.4	33.4	28.6
D	150	28.8	70.1	∞
E	150	28.8	70.1	90.7
F	180	31.2	85.7	∞

Table 1: Geometric parameters for six tested ports. L_{port} is the physical length of the port, D_c is the inner diameter at the center of the port, D_e is the inner diameter at port exit (before applying blend radii), and R_b is the bend radius for the bent ports.

Parameter	Value	Unit
R_e	3.52	Ω
L_e	0.664	mH
f_s	37.3	Hz
M_{ms}	28.08	g
K_{ms}	1.54	N/mm
R_{ms}	1.07	kg/s
Bl	7.48	N/A
S_d	120.8	cm^2
V_{as}	13.4	L
Q_{ms}	6.17	-
Q_{es}	0.413	-
Q_{ts}	0.387	-

Table 2: Measured linear free-air parameters of 6.5-inch driver used in the measurements.

the voice-coil excursion x, and the port resistance R_{ap} and port mass M_{ap} can become functions of the drive level [10]. The state X of a vented-box system can be described by the voice-coil position x, the velocity of the voice coil $\dot{x}$, the current in the voice coil i, the volume velocity of the air in the port q, and the pressure inside the box p.

$$\dot{X} = \begin{bmatrix} x & \dot{x} & i & q & p \end{bmatrix}^T \tag{1}$$

where ^{T} denotes the transpose. The evolution of the states based on an input voltage $u(t)$ can be described by the state-space equations:

$$\dot{X} = AX + Bu, \tag{2}$$

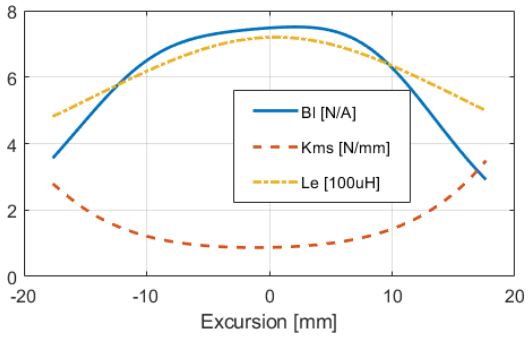

Fig. 2: Measured large-signal curves as function of driver excursion for 6.5 inch driver used in measurements. Scaling of units is shown in legend.

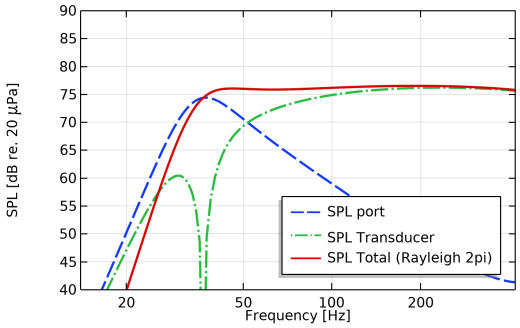

Fig. 3: System alignment at 1-V_{rms} drive level for all the ports and the 6.5-inch driver in a 12-L box. Port tuning frequency is set at 36.5 Hz, resulting in a well-tuned vented-box system.

with

$$A = \begin{bmatrix} 0 & 1 & 0 & 0 & 0 \\ -\frac{K_{ms}}{M_{ms}} & -\frac{R_{ms}}{M_{ms}} & \frac{Bl}{M_{ms}} & 0 & -\frac{S_d}{M_{ms}} \\ 0 & -\frac{Bl}{R_e} & -\frac{Le}{R_e} & 0 & 0 \\ 0 & 0 & 0 & -\frac{R_{ap}}{M_{ap}} & \frac{1}{M_{ap}} \\ 0 & K_{ab}S_d & 0 & -K_{ab} & -\frac{K_{ab}}{R_{al}} \end{bmatrix} \tag{3}$$

and

$$B = \begin{bmatrix} 0 & 0 & \frac{1}{L_e} & 0 & 0 \end{bmatrix}^T. \tag{4}$$

The box stiffness K_{ab} can be calculated by the box volume via equation (4.13) in [14]:

$$K_{ab} = \frac{1}{C_{ab}} = \frac{\rho_0 c^2}{V_{box}} = 1.18 \cdot 10^7 \text{ [N/m}^5\text{]} \tag{5}$$

with ρ_0 the density of air (1.19 kg/m^3), and c the speed of sound in air (345 m/s).

To calculate acoustic mass of the port M_{ap} we first need to estimate the effective port length L_{eff} by combining the physical port length L_{port} and the radius of a straight un-flared port tube a:

$$L_{eff} = L_{port} + \alpha\, a \tag{6}$$

with

$$\alpha = \begin{cases} 1.28 & \text{no flanged ends} \\ 1.49 & \text{one flanged end, other unflanged} \\ 1.70 & \text{both ends flanged} \end{cases} \tag{7}$$

Finally, with equation (4.7) in [14] we can estimate M_{ap}:

$$M_{ap} = \frac{\rho_0 L_{eff}}{\pi a^2} = 202\ [\text{kg/m}^4]. \tag{8}$$

Beranek gives two equations to estimate R_{ap}. Equation (4.15) in [14] is valid for $a < \frac{0.002}{\sqrt{f_b}}$ where f_b is the port tuning frequency. Equation (4.23) in [14] is valid for $\frac{0.01}{\sqrt{f_b}} < a < \frac{10}{\sqrt{f_b}}$. For ports **A** thru **E** and port tuning frequency of 36.5 Hz we get $a = \frac{0.0103}{\sqrt{f_b}}$, and thus use equation (4.23) to estimate R_{ap} to

$$R_{ap} = \frac{\sqrt{2\omega\rho_0\mu}}{pia^2}\left(\frac{L_{port}}{2} + 2\right) = 1090\ [\text{Ns/m}^5] \tag{9}$$

2.3 Linearized Large Signal Model

The aim of this work is to fit the lumped parameters from Table 2 and K_{ab}, R_{ap}, and M_{ap} to match the predictions of the LP model (1) - (4) to a measured quantity. When the driving signal is small, the lumped parameters can be assumed to be scalars, and it is a common task to match the frequency response of the predicted impedance to the frequency response of the measured impedance. However, when the applied signal voltage is large enough to drive the voice coil outside of the linear region, fitting a nonlinear model to a frequency response function (FRF) would yield erroneous results, since the FRF is a linear operation.

There are two main approaches to deal with this dilemma: Fitting the time domain response of a signal ($i(t)$, $x(t)$, etc.) or using repetitive signals and statistical approaches to separate noise and nonlinear components from the best linear approximation (BLA) of the response and then fitting the FRF of the BLA to a linear LP model. This latter approach is detailed in [15]

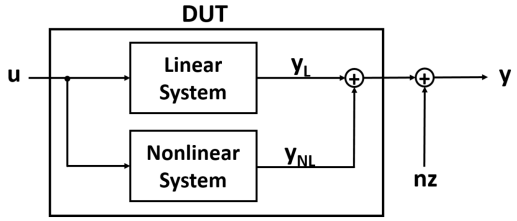

Fig. 4: General model for nonlinear DUT - u: stimulus, Y_L: linear response, Y_{NL}: nonlinear response, nz: output noise, Y: measured signal.

and has proven to be much more numerically efficient and robust for this work than attempting to fit a nonlinear signal in the time domain. We will summarize the linearization method in the following paragraphs.

A device under test (DUT) can be assumed to have an additive behavior where the nonlinear components of the response Y_{NL} are added to the linear components Y_L. The sum of Y_{NL} and Y_L, combined with measurement noise nz will produce the measured response Y [16]. This is shown schematically in Figure 4.

In order to extract the BLA response Y_L, we need to feed a repetitive signal u that is a sequence of $M \times (P+1)$ multitone signals $u_m^p(t)$ ($m = 1, 2, \cdots, M$; $p = 0, 2, \cdots, P$). The generation of an appropriate signal is described by the pseudo-code in Algorithm 1:

Algorithm 1 Generate multitone test signal

```
u = [];
for m = 1:M do
    Generate multitone u_m signal with randomized phase
    for p = 0:P do
        Concatenate u = [u,u_m]
    end for
end for
```

During the measurement, the signal u is sent to the DUT and appropriate outputs (current i, excursion x, pressure p, etc.) are recorded. The post-processing to extract the BLA of the DUT is done by subsequent averaging of the FRFs over P and M as described by the pseudo-code in Algorithm 2.

By post-processing the ratio of $Y_L = I_L/U$ in the frequency domain, Algorithm 2 will effectively linearize the FRF of the impedance of the driver at any drive

Algorithm 2 BLA extraction from nonlinear response

1: time-align y with u;
2: **for** m = 1:M **do**
3: Extract y_m that corresponds to realization u_m
4: **for** p = 1:P **do**
5: Extract u_m^p
6: Calculate FRF $\mathbf{U}_m^p = \mathscr{F}\{u_m^p\}$
7: **end for**
8: Average FRFs $\mathbf{Y}_m = \mathscr{F}\{y_m\}$ over P periods to attenuate the noise nz:

$$\mathbf{Y}_m = \frac{1}{P}\sum_{1}^{P}\mathbf{U}_m^p \tag{10}$$

9: **end for**
10: Average FRFs over M random realization to attenuate the distortion $\mathbf{Y}_{NL}$:

$$\mathbf{Y}_L = \frac{1}{M}\sum_{1}^{M}\mathbf{Y}_m \tag{11}$$

level. We exploit this feature to fit parameters of a linear LP model to the BLA of the impedance at different drive levels.

The reason for averaging only the last P periods in step 4 of Algorithm 2, instead of all $P+1$ periods is that the first period $p = 0$ contains some transient information from the $(m-1)$'th realization and we discard that information to have P periods with identical initial conditions of the loudspeaker states.

We note that a major advantage of using multitones vs sine sweeps is that the distribution of the voice-coil excursion can be predefined as described in [16], and can be approximated to typical audio content (music, speech, movie track, etc.). Using averages of sine-sweeps to extract the BLA will result in a different FRF compared to using multitones, because the distribution of voice-coil positions will be different. An analytic comparison of different stimuli on LP-values estimation will be presented in a future paper.

3 Measurements

3.1 Measurement Setup

The measurement setup consisted of an Intel i7 quad-core laptop connected to a National Instruments (NI) USB-4431 card. The card output was connected to a QSC RMX 5050a amplifier which was used on a single channel in un-bridged mode. Parallel to the 6.5-inch driver, we connected an IMP-Box by Physical Lab that measured current and voltage at the driver terminals and which was connected to the inputs of the NI card. Additionally, we placed a PCB 377A21 1/2-inch microphone in the near-field 45° from port exit at 10-cm distance from port central axis. The ports were mounted externally to the 12-L box, which had a baffle that could be mounted in a hemi-anechoic (2π) chamber. Pictures of the box and port mounted into the hemi-anechoic chamber are shown in Figure 5.

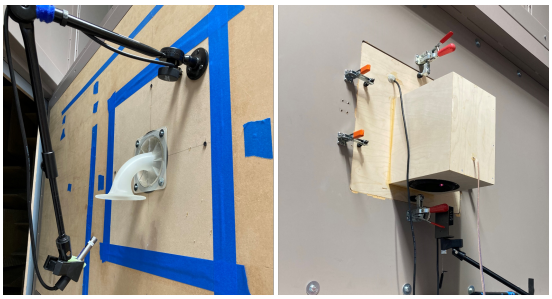

Fig. 5: Port mounted externally to a box with baffle mounted into a hemi-anechoic chamber (left), and 6.5 in driver mounted externally of the chamber (right).

3.2 Compression Measurements

A first series of measurements was conducted to determine port compression for ports **A** thru **F**. Each port was measured with an 8-second long multitone in 4-V steps between 4 V_{pk} and 72 V_{pk}. The multitone signal had a stimulus with content between 10 Hz and 200 Hz and compression was measured in that same frequency band. The compression results are shown in Figure 6. From these results we can see that the sharply bent port **C** compresses the most. The other unflared ports **A** and **B** show very little effect of bending the port with a gentle bend. The flared bent port **E** appears to start compression at higher levels compared to the unflared ports, but at very high drive levels the amount of compression is comparable to port **B**. Straight flared ports compress the least, and show significant compression relaxation, which is assumed to be due to the air-bearing effect already observed in [12]. The larger port **F** has the best performance and compresses at about a 20-V higher level than the shorter port **D**.

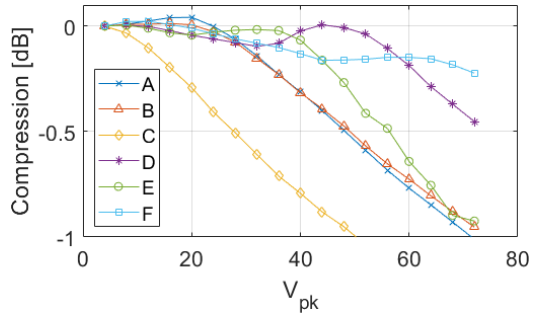

Fig. 6: Port compression measurements for ports **A** thru **F**.

3.3 Impedance Measurements

All six ports were measured with a multitone stimulus with content between 10 and 200 Hz. This range was chosen to ensure that both impedance peaks were well contained within the stimulus bandwidth. For the impedance measurements we used a multitone signal with $P = 3$ and $M = 16$, and each individual period was 500-ms long. The sampling frequency for all measurements was 48 kHz, the magnitude of the frequency content of signal was IEC weighted, and the crest factor for the individual M realizations varied between 16 and 20 dB. The peak voltage was stepped up from 4 V_{pk} to 72 V_{pk} in 4-V increments to track the changes of LP parameters with drive level. For each voltage step we fit the BLA of the measured impedance to the linear model shown in equations (1)-(4).

3.4 Fitting Algorithm

The parameter fit was performed by optimizing the values of LP q_i to reduce the root mean square error (RMSE) between the complex modeled impedance FRF $\mathbf{Z}(f,q)$ and the complex measured BLA of the impedance FRF $\hat{\mathbf{Z}}(f)$ at N log-spaced frequencies f_i between 10 Hz and 200 Hz. The loss function $\mathscr{L}(q)$ can be described by the following equation:

$$\mathscr{L}(q) = \sqrt{\frac{1}{N}\sum_{i=1}^{N}\left|\hat{\mathbf{Z}}(f_i) - \mathbf{Z}(f_i,q)\right|^2} \qquad (12)$$

In an initial trial, the fitting parameters q_i were selected to be $q = \{M_{ms}, K_{ms}, R_{ms}, K_{ab}, R_{al}, M_{ap}, R_{ap}\}$ at different V_{pk} between 4 V and 72 V. For this work, we selected to calculate the loss function at $N = 33$ log-spaced frequencies f_i between 10 and 200 Hz. Initial values $q^{(0)}$ were taken from Table 2, and equations (5), (8), and (9). The fitting was done in Matlab in two steps: first using a simplex-type optimization routine [17], and then a constrained sequential quadratic programming (SQP) [18] to fine-tune the results of the first step.

An analysis of the initial fit on the ports **A** thru **E** (port **F** was omitted because it is longer) revealed that many parameters had a very small relative standard deviation (STD) compared to the mean value, shown in Table 3. Many parameters can thus be assumed to be nearly constant across all ports and peak voltage levels. The extremely high value of R_{al} suggests that box leakage can be neglected.

q_i	units	mean $\bar{q}_i$	STD $\sigma(q_i)$	$\frac{\sigma(q_i)}{\bar{q}_i}$
Kms	N/mm	1.303	0.009	0.067
Rms	kg/s	1.139	0.018	0.016
Mms	g	29.97	0.016	0.006
Kab	N/m^5	$1.23 \cdot 10^7$	$5.23 \cdot 10^4$	0.004
Ral	Ns/m^5	$2.69 \cdot 10^{27}$	$5.32 \cdot 10^{27}$	1.972
Map	kg/m^4	233.2	2.867	0.012
Rap	Ns/m^5	3697	505.7	0.137

Table 3: Statistics of initial fit trial for ports **A** thru **E** revealed that many parameters have very low ratio of STD compared to their means and can be assumed to be constant across all peak voltage levels and ports of same length.

The mean results in Table 3 are comparable with the LPM parameters in Table 2, and equations (5) and (8). Only the mean fitted value of R_{ap} is considerably different from that given by equation (9), but $\sigma(R_{ap})$ is relatively large. It makes intuitive sense to fix M_{ms}, and K_{ab} as those should not really vary between ports or drive level. The driver suspension can exhibit creep behavior, and potentially vary with drive level. We therefore leave R_{ms} and K_{ms} as part of the set of fitting variables, together with the remaining port variables R_{ap} and M_{ap}, i.e. $q = \{K_{ms}, R_{ms}, M_{ap}, R_{ap}\}$.

For the final parameter estimation of q, we update the initial estimates $q^{(0)}$ of the previous run with the means in Table 3. The optimization routine is once again performed in two step (Nelder-Mead and SQP) as described above. The results of the final parameter fit are shown in Figure 7.

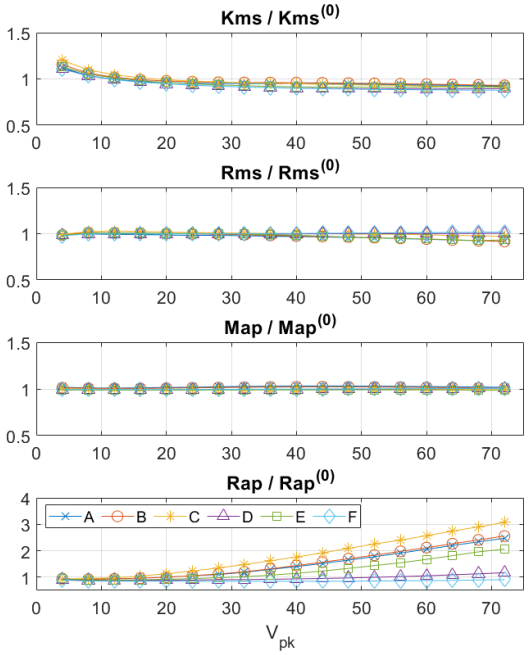

Fig. 7: Final fit of parameters K_{ms}, R_{ms}, M_{ap}, and R_{ap}, relative to their initial guesses, plotted vs peak input voltage V_{pk}. Note the different scale for R_{ap}.

From Figure 7 we can infer that R_{ms} and M_{ap} can be considered constant, as both of them vary less than 0.25 dB over all ports and all input levels. K_{ms} shows a drop of about 2 dB between input levels of 4 V_{pk} and 30 V_{pk}, and appears to reach a stationary level at higher input levels. This drop is very similar for all ports and can likely be attributed to visco-elastic effects in the driver suspension [19, 20].

Only R_{ap} shows a significant variance between the ports. Unflared ports **A**,**B**, and **C** show the most dramatic rise in R_{ap}, while flared ports without bends (ports **D** and **F**) show a much more stationary behavior for R_{ap}. Port **E**, which is flared and bent appears to fill the gap between the unflared ports and the straight flared ports. Of note is the observation that all ports show a slight drop in R_{ap} before increasing with higher input levels. This observation confirms the slight reduction in port compression at intermediate input levels, as observed by the authors in their previous paper [12], and is assumed to be a result of turbulence onset before flow separation. At intermediate levels the air at the port boundary experiences a high shear rate and

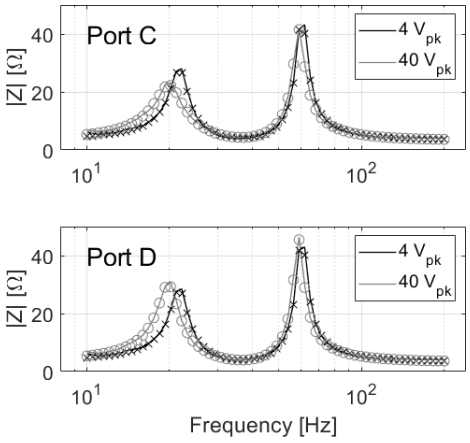

Fig. 8: Measured impedance magnitude at 4 V_{pk} (black solid line) and 40 V_{pk} (gray solid line), and the corresponding fitted impedance magnitude with LP values (x and ○ markers respectively).

starts to form turbulent vortices along the port boundary. However, the energy of these vortices is not high enough to propagate across the entire port and cause flow separation. But these vortices can act as an "air bearing," reducing the shear rate in the air outside the turbulent layer.

The relative error between measured and fitted impedance for all ports and drive levels was between 4.8% and 6.7%. Measured and fitted impedance amplitude of port **C** and **D** at different drive levels are shown in Figure 8. Port **C** shows a much more damped first peak due to the larger value of R_{ap} [21]. The shift in frequency of the first peak with higher level is due to the shift in K_{ms}, and is approximately the same for the optimally flared straight port **D** and the unflared, sharply-bent port **C**.

A nonlinear model can be used to test the fit of the estimated parameters. To obtain the nonliear $K_{ms}(x)$ curve at different drive levels we can offset the free-air $K_{ms}(x)$ curve to achieve a value of $K_{ms}(x=0)$ equal to the estimated value of K_{ms}. When trying to predict the measured current with the nonlinear LP model, we achieve relative errors between 7 and 11% for all ports and drive levels.

From Figure 6 we can infer the critical drive level V_{pk}^{crit} at which compression reaches a local minimum before increasing more severely with drive level. Using LP models with the fitted values q_i we can then calculate

the peak volume velocity q^{crit} and particle velocity u^{crit} of the air at port center for those drive levels (assuming linear flow). The velocities corresponding to onset of flow separation are shown in Table 4.

We note that V_{pk}^{crit} are not drive levels at which port air noise becomes objectionable. Listening test results in [12] suggested that ports can be driven at levels two to three times higher than V_{pk}^{crit}, but the relative values of V_{pk}^{crit} correlated well with listener preference of the ports.

Port	V_{pk}^{crit} [V]	q^{crit} [m^3/s]	u^{crit} [m/s]
A	20	$6.21 \cdot 10^{-3}$	7.0
B	20	$6.21 \cdot 10^{-3}$	7.0
C	4	$1.25 \cdot 10^{-3}$	1.4
D	44	$10.3 \cdot 10^{-3}$	21.0
E	36	$11.1 \cdot 10^{-3}$	17.1
F	60	$18.6 \cdot 10^{-3}$	24.3

Table 4: Critical drive levels V_{pk}^{crit} estimated from Figure 6, and corresponding volume velocities q^{crit} and particle velocities u^{crit}.

3.5 Noise Measurements

The pressure was recorded with the near-field microphone as shown in Figure 5. The analysis of port noise was performed in a slightly modified version to that presented in [12]. Rather than calculating the port air noise by simply taking an FFT of the measured signal and then compared the spectral content within an octave around the first port eigenfrequency f_p^1 to the total spectral content of the measured pressure, we opted to use a refined method, as described in Section 4.3.2.1 in [22] for this work. The modified method uses a multitone stimulus with $(P+1)$ periods of identical content. After discarding the first period to eliminate transient noise, an FFT is taken for each period. If noise is present in the signal, then each of the FRF will have slightly different content at the frequencies where noise is present. The variance or standard deviation of the FRFs can then be taken as a measure of noise. For the noise analysis in this work we used a multitone stimulus with content between 10 and 200 Hz and the following parameters: $P = 16$, $M = 1$, $T = 0.5$ s. The plotted standard deviation of the FRF for the six tested ports at different peak stimulus levels is shown in Figure 9. The noise plots show that all unflared ports have large peaks of noise around $f_p^1 \approx L_{eff}/(2\lambda) = 950$ Hz for the ports of 150-mm length. In addition to noise around f_p^1, the bent ports also show noise below 500 Hz that is increasing with applied stimulus level. This observation is quite significant for port **E**, and we assume it is due to the proximity of the port exit flange to the baffle of the 2π-chamber.

In order to better distill port noise as a function of drive level, we have taken the norm of the spectral content of the noise between 800 Hz and 1.6 kHz and plotted it for all ports in one figure. The results are shown in Figure 10. From those results, it appears that unsurprisingly the sharply bent and unflared port **C** performed the worst. It is showing serious noise levels at drive levels of 20 V_{pk} and above. The other unflared ports **A** and **B** start showing noise levels at similarly low drive levels, but with flatter rise towards higher drive levels. The bent and flared port **E** maintains relatively low noise levels to about 30 V_{pk}, but its noise levels rise sharply thereafter. The straight and flared ports **D** and **F** show the lowest levels of noise at low and mid drive levels, and only begin to rise to unacceptable levels above 40 V_{pk}. Flared ports overall appear to sustain higher drive levels before onset of noise, but their noise levels rise sharply above that threshold.

4 Discussion

We have presented a study to determine important LP parameters of vented boxes as function of peak drive level by use of BLA methods. Earlier studies [10] suggested that port acoustic resistance R_{ap} and acoustic mass M_{ap} are both functions of peak drive level. Here we show that M_{ap} is essentially constant for all port shapes and drive levels, and R_{ap} varies only slightly for well-designed ports. Unflared and bent ports show a strong dependence of R_{ap} with peak drive level, but straight flared ports show only minor variations of R_{ap} with respect to drive level. In fact, K_{ms} appears to vary more significantly with drive level than R_{ap} for straight flared ports. Because K_{ms} does not vary with port shape, we assume that its drift with drive level is due to driver viscoelastic suspension effects. Fitting a creep-type suspension model was not part of this study and will be left for future work. The linear LP model fit the BLA of the impedance with a relative error of approximately 5% overall, and the nonlinear LP model with the measured current with a relative error of about 7%-11% overall. These error values are fully within expected limits of LP models of vented systems [10].

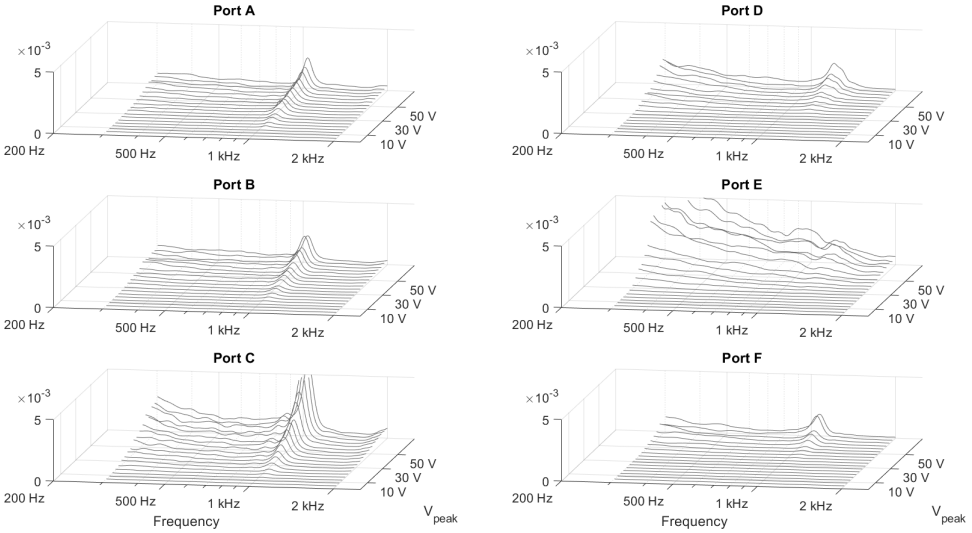

Fig. 9: FRF of port noise, as function of peak stimulus level for ports **A** thru **F**. Unflared ports show significant noise around f_p^1. Some additionally show some noise at frequencies below 500 Hz, indicating stronger distortion in addition to port air noise.

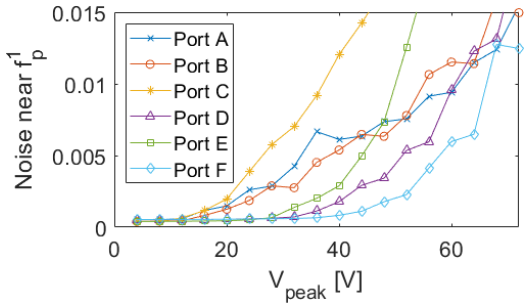

Fig. 10: Norm of noise between 800 Hz and 1.6 kHz which is near the first port eigenfrequency f_p^1.

For applications that involve nonlinear control of vented boxes [23], these findings suggest that it is not necessary to pre-tabulate values of M_{ap} and R_{ap} as function of drive level or port volume velocity as suggested in [10]. As long as ports are well-designed to eliminate flow separation and vortex shedding at typical drive levels, M_{ap} and R_{ap} vary less than 1 dB with drive level, compared to a 2 dB change of K_{ms}.

If ports are designed without flare, a gentle bend of the port does not appear to impact port performance, but a sharp bend deteriorates port output dramatically. Straight and optimally flared ports produced the least compression, port noise, and change in port parameters M_{ap} and R_{ap}. However, adding a bend to a flared port deteriorates port performance and reduces the drive level at which the port can operate linearly. At very high drive levels, flaring the ports does not appear to offer much benefit.

Samsung Electronics and Samsung Research America supported this work. The authors would like to thank the entire staff of Samsung's US Audio Lab who helped with all aspects of this research, offered insightful suggestions, and contributed to this work.

References

[1] Backman, J., "The nonlinear behavior of reflex ports," in *Audio Engineering Society Convention 98*, Paris, 1995.

[2] Vanderkooy, J., "Nonlinearities in Loudspeaker Ports," in *Audio Engineering Society Convention 104*, Amsterdam, 1998.

[3] Salvatti, A., Devantier, A., and Button, D. J., "Maximizing performance from loudspeaker ports," *Journal of the Audio Engineering Society*, 50(1-2), pp. 19–45, 2002, ISSN 0004-7554.

[4] Roozen, N. B., Bockholts, M., van Eck, P., and Hirschberg, A., "Vortex sound in bass-reflex ports of loudspeakers. Part I. Observation of response

to harmonic excitation and remedial measures," *The Journal of the Acoustical Society of America*, 104(4), pp. 1914–1918, 1998, ISSN 0001-4966, doi:10.1121/1.423760.

[5] Garcia-Alcaide, V. M., Palleja-Cabre, S., Castilla, R., Gamez-Montero, P. J., Romeu, J., Pamies, T., Amate, J., and Milan, N., "Numerical study of the aerodynamics of sound sources in a bass-reflex port," *Engineering Applications of Computational Fluid Mechanics*, 11(1), pp. 210–224, 2017, ISSN 1997003X, doi:10.1080/19942060.2016.1277166.

[6] Sivian, L. J., "Acoustic Impedance of Small Orifices," *Journal of the Acoustical Society of America*, 7(2), pp. 94–101, 1935, ISSN NA, doi:10.1121/1.1915795.

[7] Bies, D. A. and Wilson, O. B., "Acoustic Impedance of a Helmholtz Resonator at Very High Amplitude," *Journal of the Acoustical Society of America*, 29(6), pp. 711–714, 1957, ISSN NA, doi:10.1121/1.1909021.

[8] Ingard, U., "On the Theory and Design of Acoustic Resonators," *Journal of the Acoustical Society of America*, 25(6), pp. 1037–1061, 1953, ISSN NA, doi:10.1121/1.1907235.

[9] Ingard, U. and Ising, H., "Acoustic Nonlinearity of an Orifice," *The Journal of the Acoustical Society of America*, 42(1), pp. 6–17, 1967, ISSN 0001-4966, doi:10.1121/1.1910576.

[10] Button, D., Lambert, R., Brunet, P., and Bunning, J., "Characterization of nonlinear port parameters in loudspeaker modeling," in *Audio Engineering Society Convention 145*, p. 10062, New York City, 2018.

[11] Pene, Y., Horyn, Y., and Combet, C., "Non-linear acoustic losses prediction in vented loudspeaker using computational fluid dynamic simulation," in *Audio Engineering Society Convention 148*, Vienna, 2020.

[12] Bezzola, A., Devantier, A., and McMullin, E., "Loudspeaker Port Design for Optimal Performance and Listening Experience," in *Audio Engineering Society Convention 147*, p. 10311, New York City, 2019.

[13] Klippel, W., "www.klippel.de," 2020.

[14] Beranek, L. L. and Mellow, T., *Acoustics: Sound Fields and Transducers*, Academic Press, Oxford, UK, 1st edition, 2012, ISBN 9780123914217, doi:10.1016/C2011-0-05897-0.

[15] Brunet, P., DeCanio, W., Banka, R., and Yuan, S., "Use of repetitive multitone sequences to estimate nonlinear response of a loudspeaker to music," in *Audio Engineering Society Convention 143*, p. 9827, New York City, 2017.

[16] Temme, S. and Brunet, P., "A new method for measuring distortion using a multitone stimulus and non-coherence," *Journal of the Audio Engineering Society*, 56(3), pp. 176–188, 2008.

[17] Nelder, J. A. and Mead, R., "A Simplex Method for Function Minimization," *The Computer Journal*, 7(4), pp. 308–313, 1965, ISSN 0010-4620, doi:10.1093/comjnl/7.4.308.

[18] Nocedal, J. and Wright, S. J., *Numerical Optimization*, Springer Series in Operations Research and Financial Engineering, Springer New York, New York, 2nd edition, 2006, doi:10.1007/978-0-387-40065-5.

[19] Knudsen, M. H. and Jensen, J. G., "Low-Frequency Loudspeaker Models That Include Suspension Creep," *AES: Journal of the Audio Engineering Society*, 41(1-2), pp. 3–18, 1993, ISSN 00047554.

[20] Agerkvist, F. T., "Nonlinear Viscoelastic Models," in *Audio Engineering Society Convention 131*, p. 8500, New York City, 2011.

[21] Lazar, J. and Kubota, G. S., "Analysis of a Vented-Box Loudspeaker System via the Impedance Function," in *Audio Engineering Society Convention 147*, pp. E–Brief 547, New York City, 2019.

[22] Pintelon, R. and Schoukens, J., *System Identification: A Frequency Domain Approach*, John Wiley & Sons, Inc., Hoboken, NJ, USA, 2 edition, 2012, ISBN 9781118287422, doi:10.1002/9781118287422.

[23] Brunet, P., Kubota, G. S., and Li, Y., "Energy limiter for control of peak diaphragm displacement and port velocity," in *Audio Engineering Society Convention 149*, p. accepted for publication, NewYork City, 2020.